TRACKING INTRINSIC PROPERTIES OF CH 3 NH 3 PBI 3 PEROVSKITE THIN FILMS GROWN BY SPIN COATING TECHNIQUE AT…

Article · May 2017

CITATIONS
0

READS
4

2 authors:

Cliff Orori Mosiori
Technical University of Mombasa
37 PUBLICATIONS **10** CITATIONS
SEE PROFILE

John Maera
Maasai Mara University
14 PUBLICATIONS **5** CITATIONS
SEE PROFILE

Research Article

i-Proclaim.my

Asia Pac. j. energy environ.

Tracking Intrinsic Properties of $CH_3NH_3PbI_3$ Perovskite Thin Films Grown by Spin Coating Technique at Ambient Temperature

Cliff Orori Mosiori[1*], John Maera[2]

[1]Lecturer, Department of Mathematics and Physics, Faculty of Pure and Healthy Sciences, Technical University of Mombasa, Mombasa, **KENYA**
[2]Senior Lecturer, Department of Mathematics and Physical Sciences, Maasai Mara University, Narok, **KENYA**

[*]Email for Correspondence: corori@tum.ac.ke

Abstract

Methyl ammonium lead iodide has become a burgeoning class of hybrid halide perovskites of solution-processed semiconductors. Advancements in its processing and characterization underscore structural, optical, and electronic properties. They have led to the development of perovskite solar cells, photo detectors, lasers, and photo diodes with power conversion efficiencies mature to be classified as first and second-generation technologies. Characterizing forms an integral understanding the operating principles and fundamental limitations for optoelectronics applications. Studies outlined in this paper covers CH3NH3PbI3 using time-resolved pump-probe spectroscopy, X-ray diffractometry, spectrophotometry and other measurements. Thus this investigatiosn may serve as principle tool in analyzing excited state decay kinetics and optical nonlinearities in CH3NH3PbI3 thin films. It is demonstrated herein that non-resonant photoexcitation yields a large fraction of free carriers on a sub-picosecond time scale. If applied in practical optoelectronic applications then any photogenerated carriers may travel long carrier lengths before they are extracted to realize large external quantum efficiencies and efficient charge extraction. The optical constants of CH3NH3PbI3 are interpreted using ab initio calculations through models. Findings show good agreement between the optical constants derived from QSGW and those from related literature. Transition from the highest valence band (VB) to the lowest conduction band (CB) was found to be responsible for almost all the optical responses between 1.2 and 5.5 eV. It was concluded that optical constants and energy band diagrams of CH3NH3PbI3 can be used to simulate the contributions from different optical transitions to a typical transient absorption spectrum for many optoelectronic applications.

Key words

Photoexcitation, Perovskite, photogenerated, Methyl ammonium lead iodide, monovalent

11/30/2016 **Source of Support:** None | **No Conflict of Interest:** Declared

Introduction

Perovskite semiconductors are the most striking advances in the field of thin-film optoelectronic technologies (Abate etal., 2014; Yang etal., 2015) and in particular for photovoltaic applications (Lang etal., 2014; Unger etal., 2014; Xiao etal., 2014), laser diodes (Lang etal., 2014), photo detectors (Sivaram etal., 2015; Snaith etal., 2014) and even field effect transistors (Shiqiang and Walid, 2016). Current progress indicates that perovskite materials processing has enabled impressively high efficiency, inexpensive fabrication of materials by solution-processed (You etal., 2014) at room temperature on large-area substrates (Kim etal., 2012; O'Regan etal., 2015). One such a perovskite materials, is methyl ammonium lead iodide (Abate etal., 2014; Ball etal., 2013; Burschka etal., 2013; Carlos and Ignacio, 2008; Sha etal., 2015; Sivaram etal., 2015; Zuo etal., 2015). Due to its impressive unique properties (Xiao etal., 2014), its intrinsic material properties such as the grain boundaries are expected to be modified by any manufacturing process (Sivaram etal., 2015; Snaith etal., 2014) which has driven investigations on its electronic properties. Density functional theory

(DFT) has been one of the famous theories in predicting and evaluating its intrinsic parameters (Jeon etal., 2014) such as effective mass for holes and electrons that generate information about charge carrier mobility and energetics of trap states (Yang etal., 2015). A major challenge has been on the experimental front in determining structural, electronic, and optical properties. This is because $CH_3NH_3PbI_3$ is very sensitive to processing conditions. However, computational modeling (Eperon etal., 2014) has offered an alternative way using calculation theories (Haruyama etal., 2014). In this work, a number of in-depth characterizations of the electronic and in-gap properties were carried out starting with compositional and optical investigation to confirm the quality of the material. Experimentally determination of the band diagram of the semiconductor and it's proposed the applications were made. Mobility and diffusion length of both electrons and holes (Eames etal., 2015) were determined. Equally density of trap states (Shao etal., 2014) within the electronic bandgap was obtained. These helped in identifying defect states close to the valence and the conduction bands. This ensemble of determined values may provide a substantive picture of the electronic properties of $CH_3NH_3PbI_3$ which may be very essential the development of solar cells and design of light emitting diodes, light detectors, and even low cost lasers.

THEORETICAL CONSIDERATIONS

$CH_3NH_3PbI_3$ adopts a ABX_3 perovskite crystal structure, where A is methyl ammonium cation ($CH_3NH_3^+$), B, is a divalent cation (Pb^{2+}), and X is a monovalent iodide anion (I^-) (Kim etal., 2012; O'Regan etal., 2015; Xiao etal., 2014). It has an organic $CH_3NH_3^+$ part surrounded by an inorganic PbI_6 octahedral part (Lang etal., 2014).

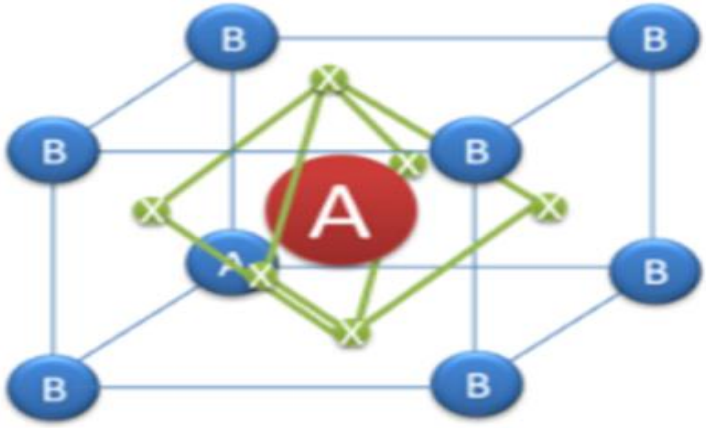

Figure 1: $CH_3NH_3PI_6$ structure: $CH_3NH_3^+$ ion surrounded by PI_6 octahedral where, A= $CH_3NH_3^+$; B = Pb, X =I (Eames etal., 2015)

The presence of an inorganic PbI_6 and an organic $CH_3NH_3^+$ in $CH_3NH_3PbI_3$ makes it a hybrid layer (Kim etal., 2012), (Lang etal., 2014; Snaith etal., 2014). At room temperature, ions have $CH_3NH_3^+$ axis aligned towards the face direction of the unit cells and the randomly change to another of the six face direction on the 3-phase line scale. Its crystal structure is shown in Figure 1 and when it is used as an absorber layer, the resulting solar cell is classified as a perovskite solar cell. It has a solubility of about 0.8g/mL at 20°C to 0.3g/mL at 80°C with average carrier mobility of $67V/cm^2.s$ and a thermal conductivity of about 0.5w/k.m at room temperature. It exhibits a series of superior opto-electronic properties that include ambipolar charge transport capacity, long carrier diffusion lengths, high optical absorption, and unique band gaps (O'Regan etal., 2015; Sivaram etal., 2015; You etal., 2014) while its structural properties present an additional layer of complexity for various applications. Calculations employing nonlocal Van der Waals correlations (Carlos and Ignacio, 2008; Minemoto and Murata, 2014) have suggested that these interactions between the organic and the inorganic parts are critical for the design of various optoelectronic applications. The effects of disorders due to distortions by rotating organic molecules at room temperature or the asymmetry of the inorganic framework leading to Rashba splitting (Eames etal., 2015) are not well understood.

METHODOLOGY

Materials

Chemicals, reagents and any other materials was used as received except the substrates that were treated before use. Anhydrous, *N*,*N*-dimethylformamide (DMF), absolute ethanol, absolute methanol (99.8%), absolute butanol (99.4%), pure formic acid, methylamine, titanium isopropoxide and lead (II) iodide (PbI_2) were purchased from Sigma-Aldrich. Concentrated hydrochloric acid was obtained from Mallinckrodt Baker suppliers. All chemicals were kept safe from any external contamination.

Substrate Preparation

The glass substrates that were used to grow the thin films were prepared according to Zhou et *al.* (2015). The procedure can be summarized as follows: substrates were cleaned by sequential sonication in acetone then in isopropyl alcohol for about 10 minutes followed by rinsing with IPA and deionized water. UV-ozone cleaning was carried out for 5 minutes.

Synthesis of Methyl ammonium formate (MAFa) solution

A volume of 25 mL of methylamine at 33% in ethanol were added to a volume of 10 mL of absolute ethanol. The mixture was then exposed to nitrogen flow in a conical flask placed in a fridge. A volume of 6 mL of 88% pure formic acid was measured and then mixed with a volume of 25 mL of pure and absolute methanol. This mixture was sucked into a 100mL plastic syringe so that it was easily to apply dropwise concentrations using a syringe. Using a syringe as an improvised pump, formic acid solution was added dropwise to the methylamine solution at a rate of 3-5 drops per second and the reaction bath stirred slowly during the addition and an extra one hour after the last drop. The flask was sealed and left 36 hours at about 0 °C in a fridge. Thereafter, the reaction product was slowly stirred at room temperature for one hour till a clear, viscous liquid was obtained. It was then stored to avoid decomposition.

Synthesis of Methyl ammonium iodide (MAI) solution

Precursor solution of methyl ammonium iodide was prepared according to You *et al.* (2014) and stored in desiccators. A precursor solution containing 30 wt% solutions of PbI_2 and CH_3NH_3 in a molar ratio 1:1 finally prepared. This was done by dissolving a solid sample of CH_3NH_3Fa in de-ionized water and stirred for about 12 hours.

Thin Film growth by Spin Coating

Thin films were prepared using spin coating as illustrated in figure A. This was by depositing at about 40 µL of 30 wt% solution and spinning it at about 2000 rpm for 30 seconds. The film thickness was controlled by using Kapton tape of various thicknesses and upon completion of the growth process; the substrates were immediately placed on a preheated stage, under nitrogen flow and annealing temperature at 130°C.

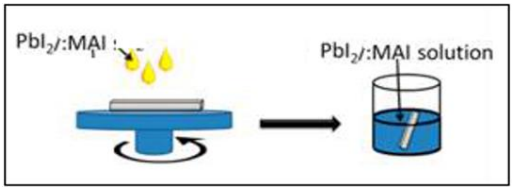

Figure 2: Spin coating illustration

Thin Film Treatment

At the end of the annealing process, the thin films were allowed to cool very slowly for about 20 minutes. After cooling down, clean residual thin films were rinsed by submerging them in butanol for 5 minutes followed by rinsing with fresh, dried butanol. The butanol rinsing agent was removed by nitrogen flow followed by heating on a hot plate at 90 -170 °C for one minute.

Thin Film Characterization

The thin films were characterized using Wide-Angle X-ray Scattering. Other techniques used included the XRD, SEM, and UV-Vis absorption measurements among others.

Wide-Angle X-ray Scattering measurements: The best result to obtain the samples occured when the samples were spin-coated at a custom-built temperature-controlled grazing incidence stage of D1 beamline, 2 with a typical transfer period of about 2 minute with the detector at 487×619 pixels with 172 µm/pixel resolution, at a distance of 92.5 mm from the sample. The x-ray wavelength was adjusted to 0.1155 nm and the incident beam angle was approximately 0.25°, well above the substrate critical angle at exposure times of less than 2 seconds. To avoid beam induced damage in the perovskite films at higher beam flux, the sample was moved perpendicular to the beam in 0.5 mm increments.

X-ray diffraction measurements: X-ray diffraction patterns (2-theta scans) were collected using a Scintag Theta-Theta X-ray Diffractometer using Cu-Kα radiation (λ=1.5405 Å). The scan speeds were adjusted such that a complete scan time was not allowed to be more than 11 minutes to minimize X-ray damage to the films because the thin films were hybrid and excess X-ray could damage the organic cations or components.

Scanning Electron Microscopy measurements: Scanning electron microscopy images were acquired first using an uncoated glass substrate and later on with coated glass substrates using a Tescan Mira3 SEM equipped with an in-lens detector.

RESULTS AND DISCUSSION

Electrical Transport trap states

To extract electrical transport in $CH_3NH_3PbI_3$, four-point and Hall Effect measurements were performed. It was found the free carrier concentration to be $n_f \approx 4 \times 10^{9}$ cm $^{-3}$ in good agreement with a near-intrinsic semiconductor (Mosconi etal., 2013; Xiao etal., 2014). The Hall coefficients revealed that the majority charge carriers were electrons with a mobility of $\mu_e \approx 50$ cm ^{2} V $^{-1}$ s $^{-1}$ with a conductivity of about $\sigma \approx 3 \times 10^{-8}$ Ω $^{-1}$. The hole mobility was measured using the space charge limited current (SCLC) technique by fitting the current–voltage (Dualeh etal., 2013; Minemoto and Murata, 2014) and obtained a hole mobility of $\mu_h \approx 65$ cm ^{2} V $^{-1}$ s $^{-1}$. These electron and hole mobilities were comparable with DFT calculations (Sha etal., 2015; Snaith etal., 2014). The effective mass as for electrons and holes were also comparable though a higher hole mobility was obtained that was attributed to improved sample preparation. Using the Einstein relation for diffusivity (Sivaram etal., 2015),

$$D = \frac{\mu k_B T}{q}$$

where, k_B is the Boltzmann constant and q, the elemental charge. Combining this quantity with the carrier lifetime τ, evaluated carrier diffusion, $L_{diff} = (D\tau)^{1/2}$ to be $L_e = L_h \approx 12$ µm, it was concluded that the high diffusion lengths and low free-carrier concentration are consequences of extremely low density of trap states.

X-ray diffraction measurements

X-ray diffraction patterns (2-theta scans) were collected using a Scintag Theta-Theta X-ray Diffractometer using Cu-Kα radiation (λ=1.5405 Å). The scan speeds were adjusted such that a complete scan time was not allowed to be more than 11 minutes to minimize X-ray damage to the films. This is because the thin films were hybrid and excess X-ray could damage the organic cations. It was observed that scattering increased with increase in temperature (figure 3). This was attributed to good crystallinity (Chen etal., 2014; Eperon etal., 2014; Sivaram etal., 2015) that made the crystals to be very compact causing more radiations to be scattered.

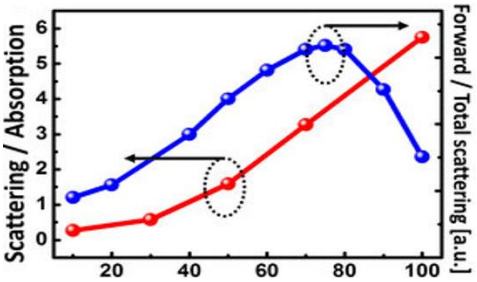

Figure 3: $MAPbI_3$ Wide-Angle X-ray Scattering

X-ray diffraction measurements

$CH_3NH_3PbI_3$ underwent structural phase transitions from orthorhombic P_{nma} to tetragonal $I4/mcm$ at ~170 K and then finally to cubic $P_{m\bar{3}m}$ at ~330 K. A tetragonal P_{4mm} phase at about 400 K was observed (Carlos and Ignacio, 2008), (Dualeh etal., 2013; Eames etal., 2015). This was attributed to its hydrogen-bonding capabilities (Mosconi etal., 2013; Snaith etal., 2014). This was an ambiguous phase transition. To precisely locate the tetragonal-to-orthorhombic phase transition point, a scan of the temperature with a range of higher resolution around the phase transition point for a 200-nm-thick thick film confirmed tetragonal-to-orthorhombic phase transition directly by the temperature-dependent SAED measurements (Lang etal., 2014; Minemoto and Murata, 2014).

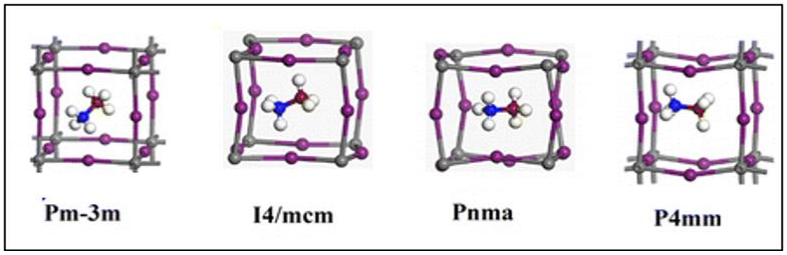

Figure 4: $MAPbI_3$ underwent structural phase transitions

Analysis on its structural evolution across these phases was carried out using *ab initio* methods (Chen etal., 2014; Meehan, 2014). It was found out that the structural phase evolved from P_{nma} to $I4/mcm$ to P_{4mm} to $P_{m\bar{3}m}$ with increasing volume. The P_{4mm} phase was quasi-cubic one with slight distortion in one direction from cubic $P_{m\bar{3}m}$ due to the rotation

of CH_3NH_3 cations (Xiao etal., 2014; Zhou etal., 2015). This unique biaxial strain on $CH_3NH_3PbI_3$ revealed that only the P_{nma} and P_{4mm} phases were energetically stable at $a < 9.14$ Å and $a > 9.14$ Å, respectively (Chen etal., 2014; Eames etal., 2015; Snaith etal., 2014). It was proposed that P_{nma}, $I4/mcm$, P_{4mm}, and $P_{m\bar{3}m}$ phases can be stable under various uniaxial strain conditions if the preparation conditions optimized. Such analysis could then provide clear structural phase transitions in $CH_3NH_3PbI_3$.

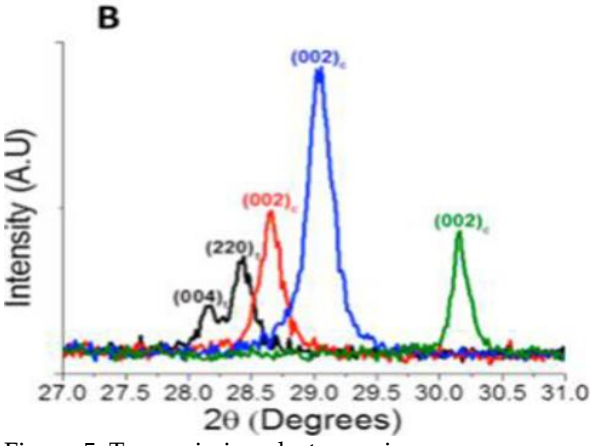

Figure 5: Transmission electron microscopy

Scanning Electron Microscopy measurements

Transmission electron microscopy image (Figure 5) showed that the patterns largely retain hexagonal shape similar with toPbI_2 before conversion. At room temperature (Fig. 3b) confirmed a single set of fourfold symmetric diffraction spots believed to be the tetragonal structure of $CH_3NH_3PbI_3$ crystals along [001] zone axis (O'Regan etal., 2015; Sivaram etal., 2015). Both first-order and second-order diffraction spots were distinguished, indicating excellent crystalline quality of the $CH_3NH_3PbI_3$. The patterns showed a set of fourfold symmetric diffraction spots with few dispersedly distributed spots indicated shown on the figure by red circles (Figure 6). Although the fourfold symmetric diffraction spots could be indexed to first-order diffraction of the orthorhombic structure along [001] zone axis, they likely belong to a different set of diffraction patterns (Sivaram etal., 2015; Xiao etal., 2014) and hence completely transited from orthorhombic phase back to tetragonal phase (Haruyama etal., 2014; Sivaram etal., 2015).

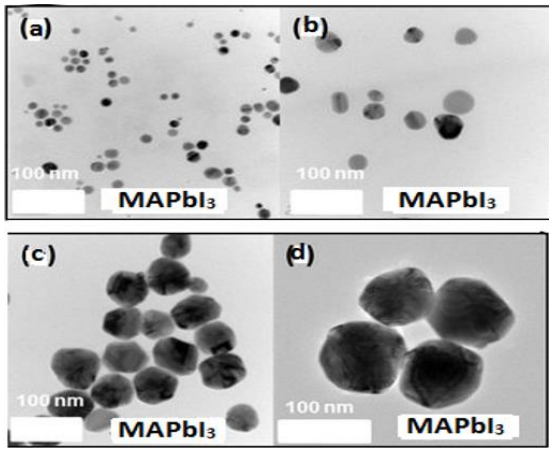

Figure 6: Low-resolution TEM image of a $MAPbI_3$ Crystals

The dispersedly distributed spot pattern showed similar features as those obtained at room temperature (Snaith etal., 2014; Wei etal., 2014; Zuo etal., 2015) implying that they only after the tetragonal-to-orthorhombic phase transition completes. Those produced at higher annealed temperatures are shown in figure 7.

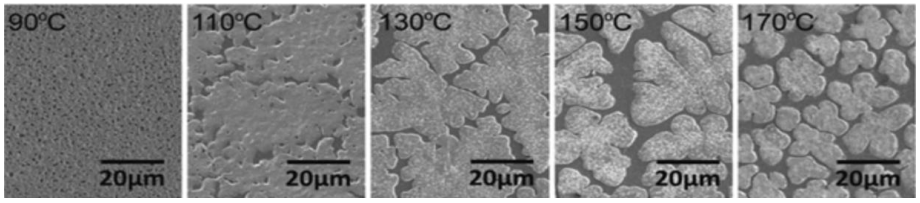

Figure 7: Films annealed at different temperatures

It was concluded that those dispersedly distributed spots might have originated from the tetragonal phase along different zone axis (Minemoto and Murata, 2014) because of the inclusions of tetragonal domains within orthorhombic phase or from the orthorhombic domains with different crystalline orientation (Wei etal., 2014). Nevertheless, the presence of dispersedly distributed spots indicated crystalline degradation quality after the tetragonal-to-orthorhombic phase transition (Chen etal., 2014; Haruyama etal., 2014; Sivaram etal., 2015; Wei etal., 2014; Zuo etal., 2015).

Optical Behavior

$CH_3NH_3PbI_3$ perovskites, optical properties of photo-generated charge carriers showed large exciton binding energy, excitonic absorption and free-excitonic emission in the visible region at room temperature. These were attributed to virtually any wavelength in the visible spectrum through adjusting the Pb atom, halide (I) or inorganic sheet thickness (Carlos and Ignacio, 2008; Dualeh etal., 2013; Snaith etal., 2014). Changing the halogen concentration affected the optical properties. Figure 8 presents the absorption spectra of the various $CH_3NH_3PbI_3$ compositions. The 1:0 indicates the $CH_3NH_3PbI_3$ perovskite with a band gap of 2.12 eV, while the 0:1 indicates a band gap of 1.51 eV. The range of band gaps, which were calculated according to Tauc plots, were between 1.51- 2.12 eV. This range was suitable for the hole conduction in free solar cells since the conduction band position was higher than most pure organic solar absorber layers (Eames etal., 2015) while the valence band position was lower than the gold work function. The exciton absorption bands shifted to short wavelength when more halide ions were introduced. The position of the absorption peak was using Pb (6s). The transitions in the $CH_3NH_3PbI_3$ perovskite were similar to the transitions in PbI_2 (Snaith etal., 2014) since the valence band of the PbI_2 was composed of Pb(6s) orbitals and I (5p) orbitals (Unger etal., 2014) while its conduction band was composed of Pb (6p) orbitals (Snaith etal., 2014). The energy level of I (4p) was lower than the energy level of Pb (6s). The peak position of $CH_3NH_3PbI_3$ was influenced and shifted to higher energy. This broad and strong light absorbance in the visible wavelength range is very in the optoelectronics (Abate etal., 2014; Marinova etal., 2015; Snaith etal., 2014). It exhibited attractive optical properties. The p–p transition and its direct bandgap resulted in a higher absorption coefficient as compared to GaAs (Sivaram etal., 2015). The high a value of about 10^5 cm^{-1} was proposed to provide a great potential if fully utilized in applications that require high photon energy absorption since larger than the bandgap and delivers high JSC from thin film devices have shown that evidence (Wilcox, 2014; Yang etal., 2015). These applications included solar cells, photo sensors, lasers, photo detectors, and photo transistors (Meehan, 2014).

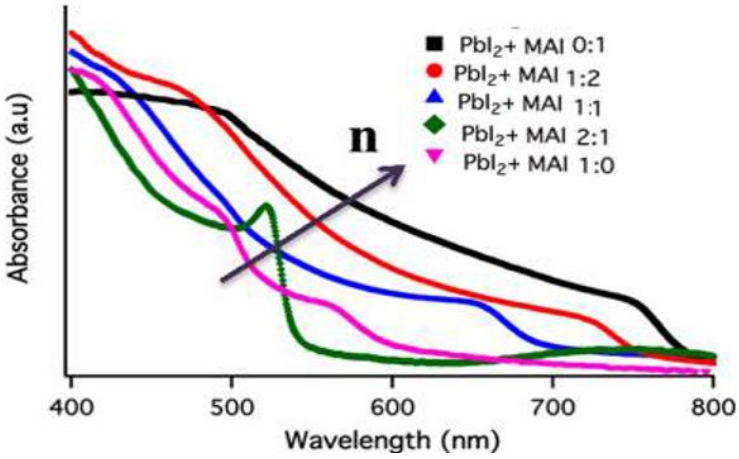

Figure 8: Absorbance of MAI

Heat treatment during annealing

Thermal annealing was found to be an essential step to ensure uniformity between the molecules, as well as the film compactness during formation (Kojima etal., 2009; Kutes etal., 2014; ACS nano). With regard to hybrid $CH_3NH_3PbI_3$ perovskite material, a delicate control of heat treatment was done to ensure fast reaction rates between the organic–inorganic component, and their various phases. Shiqiang and Walid (2016) investigated the properties of mixed halide perovskite $CH_3NH_3PbI_3$-xCl_x planar based on one-step solution processing at different annealing temperatures. Films with different film thicknesses were annealed at different temperatures ranging from 90 ^{0}C to 170 ^{0}C had similar qualities as observed (Marinova etal., 2015; Minemoto and Murata, 2014). Higher well controlled annealing temperature produced a layer with different surface coverage. This layer was recommended for use in constructing semitransparent $CH_3NH_3PbI_3$ solar cells with controlled transmission properties. The annealed films (above100 ^{0}C) produced secondary phases of PbI_2. They were attributed to originate from the decomposition of $CH_3NH_3PbI_3$ or the exchange of iodide with the $PbCl_2$.

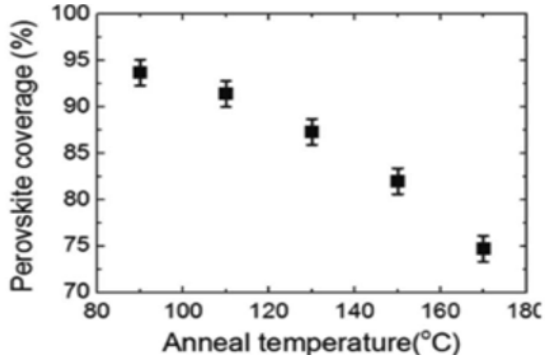

Figure 9: Annealed film coverage

This is well matched with the proposed additional side reactions (Chen etal., 2014; Minemoto and Murata, 2014; Zhou etal., 2015), as shown in Eq. (1) and (2);

$$3MAI + PbCl_2 \text{ ---------- } PbI_2 + 2MACl + MAI \quad (1)$$

$$MAPbI_3\text{---------- } PbI_2 + CH_3NH_2 + HI \quad (2)$$

Controlling the thermal annealing process was crucial factor in achieving higher performance as reported by Chen *et al.* (2014), and the stacked precursor method as reported by Xiao *et al.* (2014).

Electronic Relaxation mechanisms

Increasing quantum efficiencies (QE) was carried out by harnessing size confinement of the light absorbing in multi-exciton generation (MEG) approach (Eperon etal., 2014; Heo etal., 2015; Mosconi etal., 2013). This approach applied the concept of small bandgap semiconductor quantum dots (QD). Electronic relaxation mechanisms and their corresponding timescales allowed for a clearer picture into which relaxation processes were of greatest importance for maximum efficiency (Ball etal., 2013; Heo etal., 2015; Jeon etal., 2014; Mosconi etal., 2013; Sivaram etal., 2015). Non-radiative (NR) relaxation rates calculated by nonadiabatic dynamics and density matrix formalism were performed which produced rates on a scale of 10^{12} s^{-1} while those based on radiative (R) relaxation rates computed by estimating oscillator strengths in the independent orbital approximation were on the scale of 10^{11} s^{-1}. Finally, MEG relaxation rates computed using many-body perturbation theories were on the scale of 10^{14} $s^{-1.}$ Hence, from the computed relaxation rates, mechanism timescales trended in the order of MEG > NR > R. From these results one would expect that the MEG to be a highly probable relaxation process in the $CH_3NH_3PbI_3$ QD (Wei etal., 2014; You etal., 2014; Zuo etal., 2015).

Time-Resolved Electro-absorption Spectroscopy

A time-resolved electro-absorption spectroscopy was carried $CH_3NH_3PbI_3$ under reverse bias as illustrated in figure 10, and monitored optically the ultrafast evolution of the local counter-electric field produced by the drift of photo-generated electrons and holes in opposite directions.

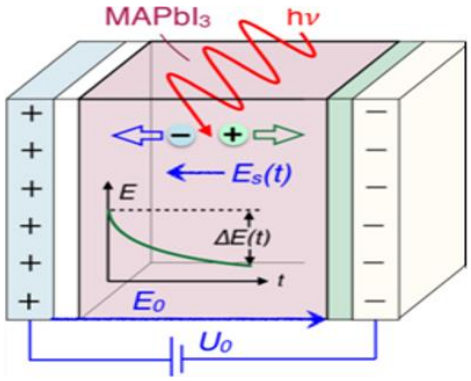

Figure 10: Time-Resolved Electro absorption

It was found that under an externally applied electric field of $|E|$ of about 10^5 V cm^{-1}, the carriers reached a separation of 40 nm within about one (1) picoseconds with an intra-grain average carrier drift mobility of $\mu\pm = 23$ cm^2 V^{-1} s^{-1}. Charge –de-trapping and migration through the entire film (Carlos and Ignacio, 2008; Lang etal., 2014; Memming and Bahnemann, 2015), owing to a trap-limited electron drift mobility was $\mu_n = 6$ cm^2 V^{-1} s^{-1} while initial charge recombination was estimated to of $n_0 \leq 2 \times 10^{16}$ cm^{-3} which was attributed to delayed charge injection (Eperon etal., 2014; Jeon etal., 2014; Shiqiang and Walid, 2016) through a poor contact junction.

DFT Computational for the weak interaction

DFT calculations performed using Vienna Ab Initio Simulation Package described the electron–ion interaction was described by the projector augmented wave (PAW) method in which the electronic orbitals 5d6s6p, 5s5p, 2s2p, 2s2p, and 1s were considered as valence orbitals for Pb, I, C, N and H atoms, respectively. The cutoff energy was picked at 400 eV and the k-space integration with a 4 × 4 × 1 k-mesh based on the Monkhorst–Pack scheme. All the structures were relaxed with conjugate-gradient algorithm until the forces on the atoms were less than 0.01 eV/A when periodic boundary conditions were applied in all three dimensions. The non-local density functional with van der Waal correction (Snaith, 2013; Xiao etal., 2014) was employed for the weak interaction. The calculated surface energies showed that the $CH_3NH_3$was thermo-dynamical more stable than the PbI_2 one under the equilibrium growth condition and that was the base in that the electronic properties of the two types of surfaces were different. The band gap of PbI_2 is smaller than that of CH_3NH_3 due to the surface Pb states and the band gaps of CH_3NH_3 decreased with increasing thickness, while band gaps of PbI_2 was insensitive to the film thickness. The calculated optical absorption coefficients suggest that both materials are effective solar energy absorbers (Eames etal., 2015; Shao etal., 2014; You etal., 2014) in the visible light spectrum.

DFT Evidence of Ferroelectric Effects

It has been proposed that temperature-dependent polarization (O'Regan etal., 2015) and dielectrics (Unger etal., 2014) may be the cause of hysteresis in hybrid solar cells of $CH_3NH_3PbI_3$. This was investigated but found no evidence of ferroelectric effect in a $CH_3NH_3PbI_3$ thin film at normal operating conditions.

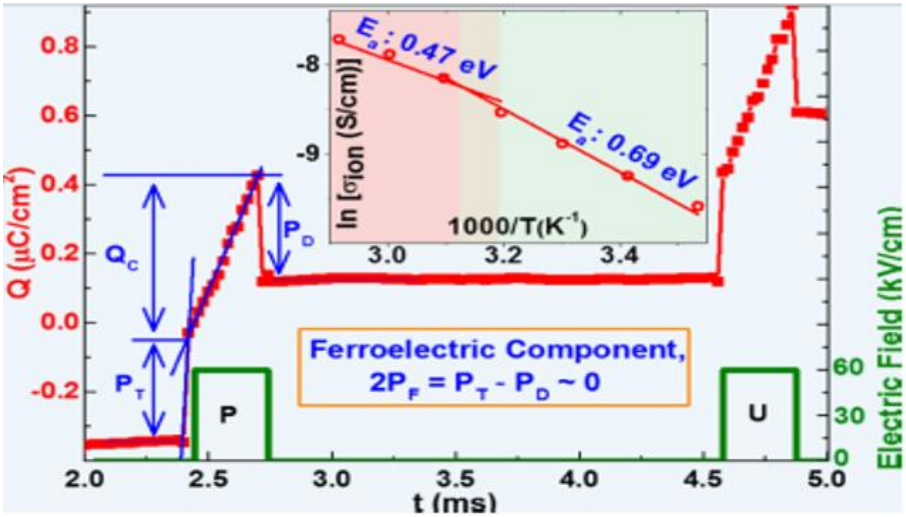

Figure 11: Ferroelectric effect in a MAPbI3

It was concluded that the proposed ferroelectric effect does not contribute to the hysteresis in Photovoltaic solar cells, whereas the large component of ionic migration observed may play a critical role in the intrinsic properties of $CH_3NH_3PbI_3$. Our temperature-based polarization and dielectric studies found out that $CH_3NH_3PbI_3$ exhibits different electrical behaviors below and above 45 °C (Burschka etal., 2013; Chen etal., 2014; Dualeh etal., 2013). This temperature of 45 °C was suggested to be the phase transition of $CH_3NH_3PbI_3$ (Abate etal., 2014; Sha etal., 2015; Zuo etal., 2015).

CONCLUSION

Thin films of $CH_3NH_3PbI_3$ were grown by spin coating and characterized. The optical constants of $CH_3NH_3PbI_3$ were interpreted using *ab initio* calculations through models and the findings showed good agreement between the optical constants with those from related literature. Transition from the highest valence band (VB) to the lowest conduction band (CB) was found to be responsible for almost all the optical responses between 1.2 and 5.5 eV. Optical constants and energy band diagrams of $CH_3NH_3PbI_3$ can be used to simulate different optical transitions for transient absorption spectrum for many optoelectronic applications. It was concluded if $CH_3NH_3PbI_3$ was to be applied for practical optoelectronic applications then its long carrier lengths could give to realize large external quantum efficiencies and efficient charge extraction in its practical devices.

ACKNOWLEDGEMENT

The authors thank members of the department of Mathematics and Physics of Technical University of Mombasa for the support they offered during the analysis of data reported herein.

REFERENCES

Abate, A.; Saliba, M.; Hollman, J.; Stranks, D.; Wojciechowski, K,; Avolio, R.; Grancini, G.; Petrozza, A.; and Snaith, J. (2014). "Supramolecular Halogen Bond Passivation of Organic–Inorganic Halide Perovskite Solar Cells". Nano Letters 14 (6): 3247–3254.

ACS nano, *Vacuum-assisted thermal annealing of $CH_3NH_3PbI_3$ for highly stable and efficient perovskite solar cells*. *9*(1), 639-646.

Ball, M.; Lee, M.; Hey, A.; and Snaith, J. (2013). "Low-temperature processed meso-superstructured to thin-film perovskite solar cells". Energy & Environmental Science 6 (6): 1739.

Burschka, J.; Pellet, N.; Moon, S.; Humphry-Baker, R.; Gao, P.; Nazeeruddin, K. and Grätzel, M. (2013). "Sequential deposition as a route to high-performance perovskite-sensitized solar cells". Nature 499 (7458): 316–319.

Carlos, F. and Ignacio G. (2008) *Revisiting the Effects of the Molecular Structure in the Kinetics of Electron transfer of Quinones: Kinetic Differences in Structural Isomers;* J. Mex. Chem. Soc. 52(1), 11-18ISSN 1870-249X

Chen, H. W., Sakai, N., Ikegami, M., & Miyasaka, T. (2014). *Emergence of hysteresis and transient ferroelectric response in organo-lead halide perovskite solar cells. The journal of physical chemistry letters*, *6*(1), 164-169.

Dualeh, A., Moehl, T., Tétreault, N., Teuscher, J., Gao, P., Nazeeruddin, M. K., & Graïtzel, M. (2013). *Impedance spectroscopic analysis of lead iodide perovskite-sensitized solid-state solar cells*. *Acs Nano*, *8*(1), 362-373.

Eames, C.; Frost, M.; Barnes, F.; Regan, C.; Walsh, A. and Islam, S. (2015). "Ionic transport in hybrid lead iodide perovskite solar cells". Nature Communications 6: 7497.

Eperon, E.; Burlakov, M.; Docampo, P.; Goriely, A. and Snaith, J. (2014). "Morphological Control for High Performance, Solution-Processed Planar Hetero-junction Perovskite Solar Cells". Advanced Functional Materials 24 (1): 151–157.

Eperon, E.; Stranks, D.; Menelaou, C.; Johnston, B.; Herz, M. and Snaith, J. (2014). "Formamidinium lead trihalide: a broadly tunable perovskite for efficient planar heterojunction solar cells". Energy & Environmental Science 7 (3): 982.

Haruyama, J., Sodeyama, K., Han, L., & Tateyama, Y. (2014). *Termination dependence of tetragonal $CH_3NH_3PbI_3$ surfaces for perovskite solar cells*. *The journal of physical chemistry letters*, *5*(16), 2903-2909.

Heo, J. H., Song, D. H., Han, H. J., Kim, S. Y., Kim, J. H., Kim, D., .. & Im, S. H. (2015). *Planar CH3NH3PbI3 perovskite solar cells with constant 17.2% average power conversion efficiency irrespective of the scan rate. Advanced Materials*, *27*(22), 3424-3430.

Jeon, N. J., Lee, H. G., Kim, Y. C., Seo, J., Noh, J. H., Lee, J., & Seok, S. I. (2014). *o-Methoxy substituents in spiro-OMeTAD for efficient inorganic–organic hybrid perovskite solar cells*. *Journal of the American Chemical Society*, *136*(22), 7837-7840.

Jeon, N.; Noh, H.; Kim, C.; Yang, S.; Ryu, S. and Seok, I. (2014). "Solvent engineering for high-performance inorganic–organic hybrid perovskite solar cells". Nature Materials 13 (9): 897–903.

Kim, H.; Lee, C.; Im, J.; Lee, K.; Moehl, T.; Marchioro, A.; Moon, S.; Humphry-Baker, R.; Yum, J.; Moser, E.; Grätzel, M. and Park, N. (2012). "Lead Iodide Perovskite Sensitized All-Solid-State Submicron Thin Film Mesoscopic Solar Cell with Efficiency Exceeding 9%". Scientific Reports 2.

Kojima, A.; Teshima, K.; Shirai, Y. and Miyasaka, T, (2009). "Organometal Halide Perovskites as Visible-Light Sensitizers for Photovoltaic Cells". Journal of the American Chemical Society 131 (17): 6050–6051.

Kutes, Y., Ye, L., Zhou, Y., Pang, S., Huey, B. D., & Padture, N. P. (2014). *Direct observation of ferroelectric domains in solution-processed $CH_3NH_3PbI_3$ perovskite thin films*. *The journal of physical chemistry letters*, *5*(19), 3335-3339.

Lang, L.; Yang, J.; Liu, H.; Xiang, J. and Gong, G. (2014). *First-principles study on the electronic and optical properties of cubic ABX_3 halide perovskites.* Physics Letters A 378 (3): 290–293.

Marinova, N., Tress, W., Humphry-Baker, R., Dar, M. I., Bojinov, V., Zakeeruddin, S. M., & Graïtzel, M. (2015). *Light harvesting and charge recombination in $CH_3NH_3PbI_3$ perovskite solar cells studied by hole transport layer thickness variation*. *ACS nano*, *9*(4), 4200-4209.

Meehan, C. (2014). *"Getting the lead out of Perovskite Solar Cells"*. Solar Reviews.

Memming, R., & Bahnemann, D. (2015). *Semiconductor electrochemistry*. John Wiley & Sons.

Minemoto, T. and Murata, M., (2014). "Device modeling of perovskite solar cells based on structural similarity with thin film inorganic semiconductor solar cells". Journal of Applied Physics 116 (5): 054505.

Mosconi, E.; Amat, A.; Nazeeruddin, K.; Grätzel, M. and Angelis, F. (2013). "First-Principles Modeling of Mixed Halide Organometal Perovskites for Photovoltaic Applications". The Journal of Physical Chemistry C 117 (27): 13902–13913.

O'Regan, B. C., Barnes, P. R., Li, X., Law, C., Palomares, E., & Marin-Beloqui, J. M. (2015). *Optoelectronic studies of methylammonium lead iodide perovskite solar cells with mesoporous TiO_2: separation of electronic and chemical charge storage, understanding two recombination lifetimes, and the evolution of band offsets during J–V hysteresis*. *Journal of the American Chemical Society*, *137*(15), 5087-5099.

Sha, E.; Ren, X.; Chen, L.; and Choy, H. (2015), "The efficiency limit of $CH_3NH_3PbI_3$ perovskite solar cells". Appl. Phys. Lett. 106 (22): 221104.

Shao, Y., Xiao, Z., Bi, C., Yuan, Y., & Huang, J. (2014). *Origin and elimination of photocurrent hysteresis by fullerene passivation in $CH_3NH_3PbI_3$ planar heterojunction solar cells. Nature communications*, *5*.

Shiqiang Luo and Walid A. Daoud (2016) *Crystal Structure Formation of* $CH_3NH_3PbI_{3-x}Cl_x$ *Perovskite,* Materials 2016, 9, 123

Sivaram, V.; Stranks, D. & Snaith, J. (2015). "Outshining Silicon". Scientific American: 44–46.

Snaith, J. (2013). "Perovskites: The Emergence of a New Era for Low-Cost, High-Efficiency Solar Cells". The Journal of Physical Chemistry Letters 4 (21): 3623–3630.

Snaith, J.; Abate, A.; Ball, M.; Eperon, E.; Leijtens, T.; Noel, K.; Wang, T.; Wojciechowski, K.; Zhang, W. and Zhang, W. (2014). "Anomalous Hysteresis in Perovskite Solar Cells". The Journal of Physical Chemistry Letters 5 (9): 1511–1515.

Unger, L.; Hoke, T.; Bailie, D.; Nguyen, H.; Bowring, R.; Heumuller, T.; Christoforo, G. and McGehee, D. (2014). "Hysteresis and transient behavior in current-voltage measurements of hybrid-perovskite absorber solar cells". Energy & Environmental Science 7 (11): 3690–3698.

Wei, J., Zhao, Y., Li, H., Li, G., Pan, J., Xu, D., & Yu, D. (2014). *Hysteresis analysis based on the ferroelectric effect in hybrid perovskite solar cells. The journal of physical chemistry letters*, *5*(21), 3937-3945.

Wilcox, K. (2014). "Solar Researchers Find Promise in Tin Perovskite Line". Civil Engineering.

Xiao, Z.; Bi, C.; Shao, Y.; Dong, Q.; Wang, Q; Yuan, Y.; Wang, C.; Gao, Y. and Huang, J. (2014). "Efficient, High Yield Perovskite Photovoltaic Devices Grown by Interdiffusion of Solution-Processed Precursor Stacking Layers". Energy & Environmental Science 7 (8): 2619.

Yang, B.; Dyck, O.; Poplawsky, J.; Keum, J.; Puretzky, A.; Sanjib, D.; Ivanov, I.; Rouleau, C.; Duscher, G.; Geohegan, D. and Xiao, K. (2015). "Perovskite Solar Cells with Near 100% Internal Quantum Efficiency Based on Large Single Crystalline Grains and Bulk Heterojunctions". J. Am. Chem. Soc. 137 (29): 9210–9213.

You, J.; Hong, Z.; Yang, M.; Chen, Q; Cai, M; Song, T; Chen, C.; Lu, S. and Liu, Y. (2014). "Low-Temperature Solution-Processed Perovskite Solar Cells with High Efficiency and Flexibility". ACS Nano 8 (2): 1674–1680. ISSN 1936-0851.

Zhou, Y.; Yang, M.; Wu, W.; Vasiliev, L.; Zhu, K. and Padture, P. (2015). "Room-temperature crystallization of hybrid-perovskite thin films via solvent–solvent extraction for high-performance solar cells". J. Mater. Chem. A 3 (15): 8178–8184.

Zuo, L., Gu, Z., Ye, T., Fu, W., Wu, G., Li, H., & Chen, H. (2015). *Enhanced photovoltaic performance of $CH_3NH_3PbI_3$ perovskite solar cells through interfacial engineering using self-assembling monolayer. Journal of the American Chemical Society*, *137*(7), 2674-2679.

-- 0 --

Google Scholar: https://goo.gl/0tQ6Lt